

pubs.acs.org/acscatalysis Research Article

Hydrothermally Stable and Regenerable Molybdenum-Zeolite Catalysts for Nonoxidative Conversion of Methane to Dihydrogen and Ethene

Ángel N. Santiago-Colón, Hien Pham, Ayotunde Alabi, David Hibbitts, Abhaya Datye, and Rajamani Gounder*



Cite This: ACS Catal. 2025, 15, 17568-17580



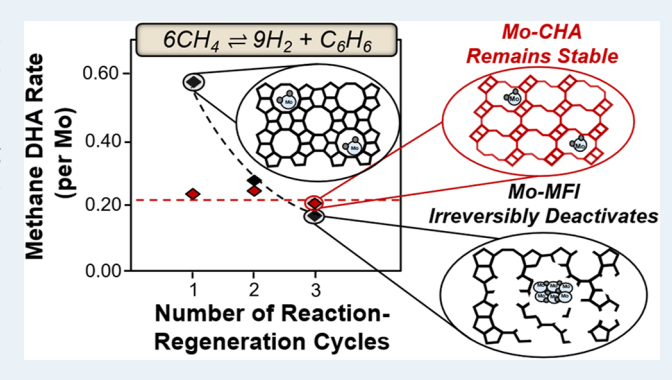
ACCESS

III Metrics & More

Article Recommendations

s Supporting Information

ABSTRACT: Designing Mo-zeolite catalysts that retain structural stability over many reaction—regeneration cycles is a challenge in developing practical methane dehydroaromatization (DHA) routes to produce dihydrogen, ethene, and aromatics. Mo-MFI zeolites typically used for methane DHA irreversibly deactivate during regeneration due to framework dealumination and structural degradation. Here, we synthesize Mo supported on small-pore zeolites (e.g., CHA, AEI, RTH), which are more durable than MFI under hydrothermal aging conditions (>823 K, >2 kPa H₂O). Methane DHA forms H₂ and ethene at equivalent rates on Mo-CHA and Mo-MFI. Benzene formation rates (per Mo) increase with decreasing crystallite size, indicating that rates are intracrystal-line-diffusion limited in CHA frameworks, consistent with density



functional theory (DFT) estimates of benzene diffusion barriers in CHA 8-membered ring (8-MR) windows. Initial DHA rates (per Mo) remain invariant on Mo-CHA after successive reaction—regeneration cycles (>10), supported by high-resolution transmission electron microscopy (HRTEM) and quantitative site characterization data showing minimal site or structural degradation on Mo-CHA, in sharp contrast to the systematic decrease in rates and structural degradation observed on Mo-MFI. This work reports materials that can be fully regenerable under potential industrial conditions and provides structure—function relations between catalyst properties and DHA rates, selectivity, and long-term stability.

KEYWORDS: Mo-zeolite, stability, methane dehydroaromatization, regeneration, hydrogen

1. INTRODUCTION

Methane dehydroaromatization (DHA) is a nonoxidative route to convert methane into dihydrogen, ethene, and aromatics (e.g., benzene, naphthalene), which can be catalyzed to nearequilibrium conversion with high (60-80%) aromatics and H₂ selectivity by molybdenum supported on MFI zeolites (Mo-MFI).¹⁻³ Mo-MFI zeolites deactivate during reaction due to the formation of carbonaceous deposits, which can be managed using a continuous reaction and regeneration process in a circulating fluidized bed reactor. 4-6 Techno-economic analyses of envisioned commercial methane DHA applications indicate that preserving catalyst stability through successive reactionregeneration cycles is one of the critical bottlenecks preventing commercialization, as the internal rate of revenue significantly decreases (~50-60%) upon considering the costs associated with replacing deactivated catalysts.7 Thus, catalyst design efforts to improve long-term catalyst stability and structural durability throughout successive methane DHA reactionregeneration cycles would address barriers to commercial implementation, 6-8 while providing generalizable insights into structure—function relations describing how metal-zeolite materials evolve throughout deactivation and regeneration treatments encountered in practice.

Mo-MFI irreversibly deactivates with increasing numbers of reaction—regeneration cycles due to framework dealumination and structural collapse as determined by XRD, causing Mo sublimation into the gas phase and formation of agglomerated aluminum molybdate domains that do not carburize and are thus inactive for methane DHA. Recently, we showed using $\rm H_2$ temperature programmed reduction (TPR), $^{27}\rm Al$ solid-state NMR, and NH $_3$ titration of residual H $^+$ sites that the loss of framework Al centers resulting from exposure to hydrothermal aging conditions during oxidative regeneration

Received: July 9, 2025
Revised: September 9, 2025
Accepted: September 26, 2025



protocols (>823 K) leads to a decrease in the number of H⁺ sites and, in turn, ion-exchanged Mo species that serve as precursors to Mo (oxy-)carbide active sites for DHA.¹³ Thus, preserving framework Al centers and associated H⁺ sites in the zeolite support through successive reaction and regeneration cycles is critical to the design of catalysts that can retain sufficient methane DHA reactivity and benzene yields for practical applications. Strategies to prolong the useful lifetime of Mo-MFI zeolites through successive reaction-regeneration cycles include modifying the duration and temperature of methane DHA reaction and regeneration protocols, which influences the extent of dealumination in the zeolite support. 11,14 Another strategy to extend Mo-MFI lifetime is to decrease the Mo loading, relative to framework Al or associated H⁺ sites available initially on the zeolite support, which effectively increases the number of cycles required to dealuminate the zeolite to an extent where insufficient H+ binding sites exist to fully redisperse Mo during regeneration. 10

Here, we propose an alternative material design approach to synthesize small-pore 8-membered ring (8-MR) zeolite frameworks, such as chabazite (CHA), which have been shown to retain structural integrity during hydrothermal aging conditions in commercial diesel emissions aftertreatment systems for NO_x selective catalytic reduction (SCR). ^{15,16} We show that methane DHA forms H2, ethene, and ethane at equivalent yields on Mo-CHA and Mo-MFI. Although aromatic formation rates and yields are lower ($\sim 5-6\times$) in Mo-CHA than in Mo-MFI due to intrazeolite diffusional constraints imposed by the CHA framework, we report crystal engineering (e.g., modifying crystallite size and morphology) and reaction engineering strategies (e.g., H2 cofeeds) to influence aromatics formation rates and selectivity to gas-phase hydrocarbon products, respectively. Importantly, cyclic reaction-regeneration treatments demonstrate that aromatic formation rates remain invariant on Mo supported on smallpore zeolites (e.g., CHA, RTH, AEI), in sharp contrast to the systematic decreases in rates observed after cyclic regeneration of Mo-MFI that eventually become less reactive than Mo-CHA zeolites. This work demonstrates that Mo supported on smallpore zeolites can be fully regenerated and their design optimized to produce H₂, ethene, and aromatics.

2. METHODS

2.1. Zeolite Synthesis and Characterization. CHA, nano-CHA, RTH, and AEI zeolites were synthesized following previously reported procedures and are detailed in Section S1 of the Supporting Information. 17,18 Nanosheet-CHA and mesoporous-CHA were synthesized by modifying CHA recipes with the addition of organosilane amphiphilic surfactant dimethyloctadecyl[3-(trimethoxysilyl)propyl]ammonium chloride (TPOAC, 42 wt % in methanol, Sigma-Aldrich; details in Section S1 of the Supporting Information). Synthesized zeolites were characterized by powder X-ray diffraction (XRD), Ar adsorption isotherms (87 K), and elemental analysis to determine the zeolite framework, measure micropore volume, and measure Mo, Si, and Al content, respectively. Details on characterization techniques are provided in Section S2 of the Supporting Information. Commercial MFI zeolite (CBV 2314, Si/Al = 11.5) was obtained from Zeolyst International.

2.2. Mo-Zeolite Synthesis and Characterization of Mo Speciation. Mo supported in CHA, MFI, RTH, and AEI zeolites were synthesized by solid-state exchange (SSE) using

protocols described in our previous work.¹³ In brief, MoO_3 (Sigma-Aldrich, 99.9%) and each zeolite (in its NH_4^+ form) were mixed with a mortar and pestle for 0.4–0.5 h, followed by treatment in air $(1.67 \text{ cm}^3 \text{ (g zeolite)}^{-1} \text{ s}^{-1}$, Air Zero, Indiana Oxygen) in a muffle furnace to 823 K for 6 h $(0.0167 \text{ K s}^{-1})$.

Fresh and spent Mo-zeolites were characterized by using H₂ temperature programmed reduction (TPR), in situ X-ray absorption spectroscopy (XAS), and transmission electron microscopy (TEM). H₂ TPR protocols were adapted from our previous work. 13 Protocols for selective NH3 titration of H+ sites on zeolite materials containing other binding sites (e.g., Lewis acid sites in Mo-zeolites) were reported in our previous work¹³ and adapted from methods developed by Di Iorio et al. to use NH₃ to selectively titrate H⁺ sites in Cu-zeolites. ¹⁹ In situ XAS experiments were performed at the Advanced Photon Source (APS) at Argonne National Laboratory (ANL) and at Brookhaven National Laboratory (BNL, Sector 8-ID). TEM imaging was recorded in an annular dark field (ADF-), annular bright field (ABF-), and high-resolution (HR-) mode. Full description of these techniques is discussed in Section S2 of the Supporting Information.

2.3. Methane DHA Kinetic Measurements and Cyclic Reaction–Regeneration Protocols. Methane DHA kinetic measurements were performed in a tubular reactor and experimental setup described in our previous work. Reactions were performed at 950 K and 90 kPa CH₄ (unless otherwise noted) and contact times >8 mol Mo·s (mol CH₄)⁻¹. Reactants and products were quantified using a gas chromatograph with a flame ionization detector for hydrocarbons and a thermal conductivity detector for light gases. H₂ cofeed (5–13 kPa) experiments were performed by mixing a stream of 90/10% CH₄/Ar (v/v%, Certified Mixture, Indiana Oxygen) with a stream of pure H₂ (UHP, Indiana Oxygen). Expressions to calculate benzene forward formation rates and carbon product turnover numbers are discussed in Section S3 of the Supporting Information.

Sequential reaction—regeneration cycles were performed by running methane DHA (950 K) until benzene forward rates deactivated ~80–90% of the initial rate. The reactor was cooled to 823 K with flowing He (UHP, 99.999%, Indiana Oxygen) for 0.5–2 h before introducing air (0.3 cm³ s⁻¹, Air Zero, Indiana Oxygen) at 823 K for catalyst regeneration. Accelerated aging procedures were performed by introducing water (20 kPa) to air during regeneration at 923 K for 8 h (details in Section S3 of the Supporting Information). This protocol emulates strategies used in the emissions control (e.g., NO_x SCR) literature to simulate catalyst field aging in laboratory conditions, which allows assessing new catalyst formulations in a shorter time. 21,22

2.4. Diffusion Barrier Calculations Using Density Functional Theory. Density functional theory (DFT) calculations were performed using the Vienna *Ab initio* Simulation Package (VASP), $^{23-26}$ as implemented in the Computational Catalysis Interface (CCI). The Perdew–Burke–Ernzerhof (PBE) form of the generalized gradient approximation was employed to estimate exchange and correlation energies, $^{24-26}$ with dispersive interactions modeled using the DFT-D3 method with Becke–Johnson damping. $^{27-29}$ Planewave basis sets were constructed using the projector augmented wave (PAW) method with an energy cutoff of 400 eV, and the Brillouin zone was sampled only at the Γ -point. 30 Structural optimizations were performed using a multistep process. In the first step, structures were electroni-

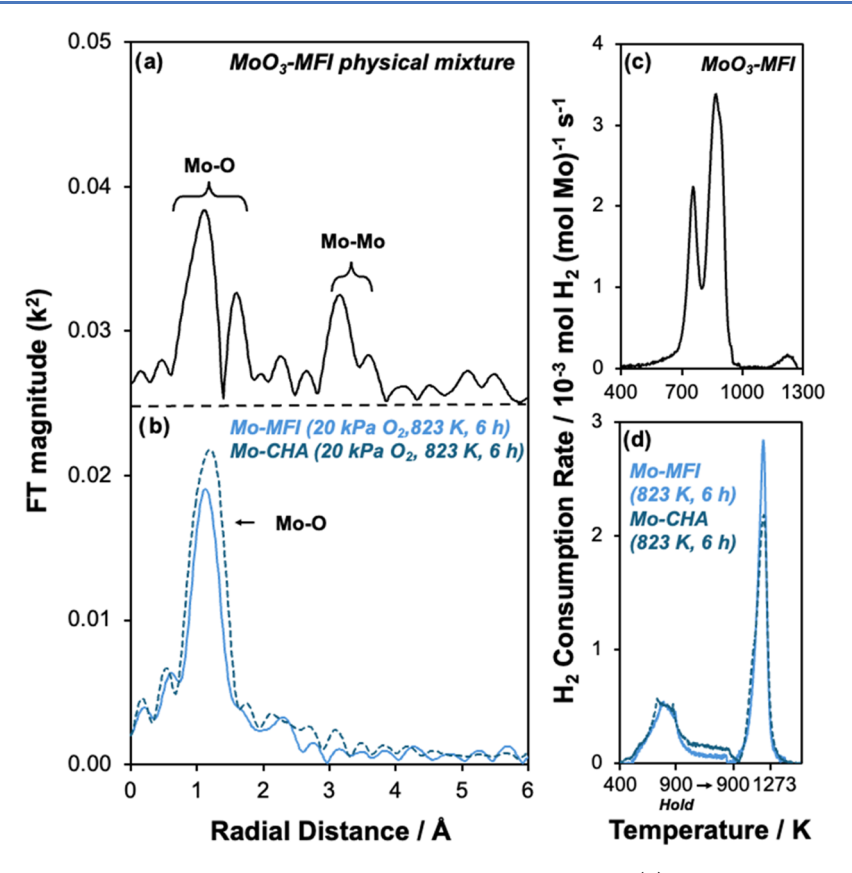


Figure 1. (a) Mo K-edge EXAFS of a MoO₃–MFI physical mixture after air treatment to 473 K, (b) EXAFS of Mo-MFI (light blue solid trace) and Mo-CHA (dark blue dashed trace) after 20 O₂ kPa treatment at 823 K, (c) H₂ TPR profile of MoO₃–MFI physical mixture after air treatment to 473 K adapted from Santiago-Colón and Gounder¹³ Copyright 2024 Journal of Catalysis, (d) H₂ TPR profile of Mo-MFI (Mo/Al = 0.10; light blue solid trace) adapted from Santiago-Colón and Gounder¹³ Copyright 2024 Journal of Catalysis, ¹³ and Mo-CHA (Mo/Al = 0.15; dark blue dashed trace) after high-temperature (823 K, 6 h) air treatment. Data were collected at ANL.

cally converged until energy varied by $<10^{-4}$ eV between iteration, with forces calculated using a Fast Fourier Transform (FFT) grid set to 1.5 times the plane wave cutoff. In the second step, wave functions were converged to $<10^{-6}$ eV, with forces on all atoms converged to <0.05 eV Å⁻¹. No atoms were constrained during calculations. ²³ Calculations involving the zeolite structure were performed with periodic structures of the MFI and CHA frameworks.

Diffusion pathways were modeled utilizing the Nudged Elastic Band (NEB) 31 and Dimer methods. 32 NEB calculations involved 16 images along the diffusion pathway and employed a fast Fourier transform (FFT) grid set to 1.5 times the planewave cutoff to ensure accurate energy convergence. NEBs were converged so that the maximum force in all atoms in each image is <0.15 eV Å $^{-1}$. Transition state searches using the Dimer method were initiated using these more refined NEB results. Dimer optimization followed a two-step process analogous to that of the minimum-point optimizations, 32 until the forces on all atoms converged to <0.05 eV Å $^{-1}$.

3. RESULTS AND DISCUSSION

3.1. Synthesis of Mo-CHA and Characterization of Mo Speciation and Dispersion. Mo-CHA catalysts have been studied for methane DHA, yet materials reported to date show very low benzene yields (<0.5%) and selectivity (<3%), $^{33-35}$ which have been attributed to both low Mo dispersion in CHA evidenced by scanning electron microscope (SEM) images of MoO₃ clusters formed at exterior surfaces of CHA crystallites

after high-temperature air treatments³⁵ and to diffusion constraints imposed by the 8-MR window apertures (~0.38 nm diam.) that are smaller than the kinetic diameter of benzene (~0.59 nm diam.). To address the first issue, we synthesized Mo-CHA and characterized the Mo species formed using X-ray absorption spectroscopy (XAS) and H₂ TPR. Typical synthesis of Mo-MFI involves depositing Mo oxide precursors onto MFI supports, followed by a hightemperature (>773 K) air treatment to facilitate Mo exchange reactions with zeolitic H+ sites to form ion-exchanged Mo species (i.e., $[MoO_2]^{2+}$, $[Mo_2O_5]^{2+}$, $[MoO_2OH]^+$). $^{36-39}$ Ionexchanged Mo species are carburized by methane at high temperatures (>950 K) during the initial time-onstream^{36,40-42} to form DHA-active Mo (oxy-)carbides domains. 43,44 Mo dispersion on MFI zeolites depends on both the number and proximity of H+ sites, where Mo exchange preferentially occurs at proximal H+ sites (Al-Al distance <0.7 nm) to form [MoO₂]²⁺ and [Mo₂O₅]²⁺ species. 13,39,45 Once proximal H⁺ sites have been exchanged with Mo (typically at Mo/Al > 0.4), the remaining isolated H⁺ sites would nominally exchange [MoO₂OH]⁺, but such species have been predicted by ab initio thermodynamic calculations to be thermodynamically unfavored relative to aluminum molybdate clusters, which form upon reaction with extraframework Al moieties and are inactive for DHA. 10,13,37 Therefore, we synthesized Mo-CHA materials with low Mo content (Mo/Al = 0.15-0.25, synthesis and characterization methods described in Section S1 and Section S2, respectively

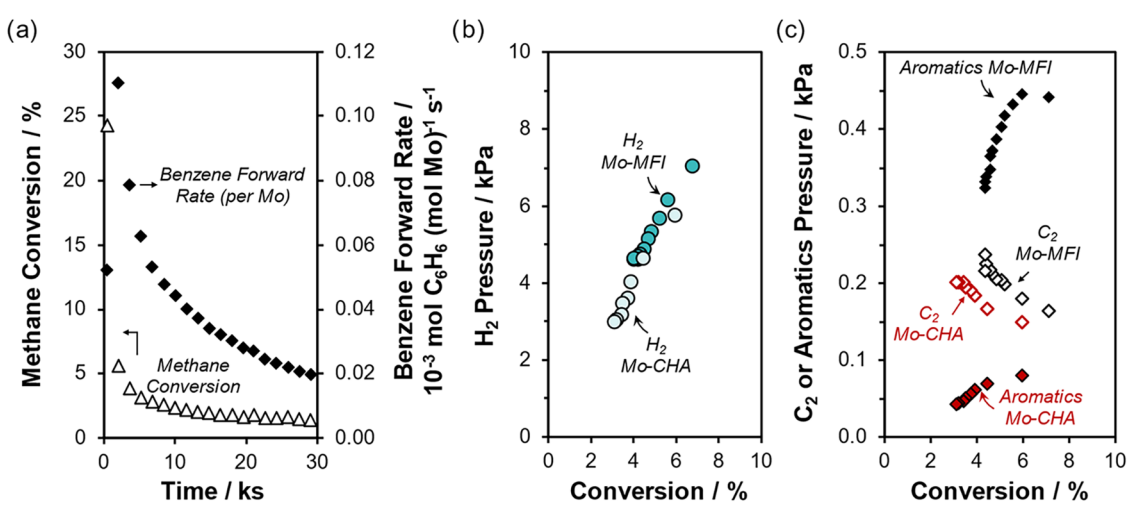


Figure 2. (a) Methane conversion (triangles) and benzene forward rate (diamonds) measured on Mo-CHA during time-on-stream. (b) $\rm H_2$ pressure in reactor effluent as a function of methane conversion measured on Mo-MFI (dark turquoise circles) and Mo-CHA (light turquoise circles) during deactivation. (c) Aromatics (solid diamonds) and $\rm C_2$ (open diamonds) pressures in reactor effluent as a function of methane conversion measured on Mo-MFI (black symbols) and Mo-CHA (red symbols) during deactivation.

of the Supporting Information) to maximize the formation of ion-exchanged Mo at proximal H^+ sites and minimize the formation of aluminum molybdate domains and compared this to a Mo-MFI material with similar Mo content and postsynthetic treatment.

Figure 1a shows the extended X-ray absorption fine structure (EXAFS) analysis of a MoO₃-MFI physical mixture, where peaks at 1.5 and 3.2 Å are observed for first-shell Mo-O and second-shell Mo-Mo scattering, respectively, resembling EXAFS spectra of MoO₃ clusters.⁴⁶ In contrast, EXAFS spectra of Mo-MFI and Mo-CHA after high-temperature (823 K) air treatment (Figure 1b) show a single peak at 1.2 Å, indicating that MoO_x clusters have been dispersed into Mo⁶⁺ species (XANES spectra shown in Figure S2 and edge energy in Table S1, Supporting Information) and are consistent with XAS experiments with Mo-CHA reported by Agote-Arán et al. 35,41,47 Titration of residual H⁺ sites on Mo-CHA (Table S6, Supporting Information) shows a decrease in H⁺ site density, indicating that MoO_x species exchanged onto H⁺ sites to form ion-exchanged Mo species, as has been observed in Mo-MFI after high-temperature air treatments. 37,38,44

H₂ TPR profiles of MoO₃-MFI before air treatment (Figure 1c) show stepwise Mo⁶⁺→Mo⁴⁺ reduction followed by Mo⁴⁺ → Mo⁰ reduction, characteristic of H₂ TPR profiles of bulk $\mathrm{MoO_{3}.^{48}}$ The reduction profile of Mo-CHA samples after 823 K air treatment (Figure 1d) also shows a stepwise reduction but with features centered at ~800 and ~1260 K, as also observed in the Mo-MFI (Figure 1d) TPR profile. We have reported that the high-temperature reduction feature (1260 K) is a signature of ion-exchanged Mo species and can be used to monitor Mo structural changes during reaction-regeneration cycles.¹³ Quantification of the total H₂ consumed (per Mo) is ~2.9, consistent with full reduction of $Mo^{6+} \rightarrow Mo^{0}$. Taken together, these XAS and TPR data suggest that, similar to Mo-MFI materials, high-temperature air treatment protocols are sufficient to fully disperse Mo species onto the CHA zeolite support as long as the amount of Mo does not exceed the number of available H⁺ exchange sites.

3.2. Methane DHA Kinetic Measurements on Mo-CHA and Assessment of Benzene Diffusion Rates Using DFT-Calculated Diffusion Barriers. Methane DHA reactions

were performed using Mo-CHA (1.9-2.8 wt % Mo), and forward rates of benzene formation (per Mo) were calculated using formalisms derived by Razdan et al. (Section S3, Supporting Information).⁴³ Low hydrocarbon balance values (<0.1) and CO formation (Figure S5, Supporting Information) during early time-on-stream (<1 ks) indicate carburization of ion-exchanged Mo species into Mo (oxy-)carbides, which are DHA-active sites, and carbon deposition on zeolitic surfaces. 36,49 In situ XANES of Mo-CHA exposed to methane at 973 K shows a shift to lower edge energy characteristic of Mo₂C (Figure S2 and Table S1, Supporting Information), further evincing formation of Mo (oxy-)carbide domains. 40,50,51 Methane conversion and benzene formation rates (per Mo) decrease with time-on-stream (Figure 2a), while hydrocarbon balance values increase to a steady-state value of ~0.20. The carbon unaccounted for in gaseous products remains deposited on the zeolite and leads to deactivation, consistent with Raman spectra of spent Mo-CHA showing bands associated with graphitic carbon and polyaromatic species.¹⁷ The benzene selectivity measured here on Mo-CHA is higher than reported by Agote-Arán et al. and Kosinov et al. (Table 1), which we hypothesize reflects the

Table 1. Benzene Selectivity Measured on Mo-CHA Catalysts in the Literature and This Work

reference	Mo (wt %)	highest benzene selectivity (%)
Agote-Arán et al. ^{35a}	4.0	3
Kosinov et al. ^{34b}	5.0	<1
this work	2.8	12

^aReaction conditions: 973 K, 50/50 (v/v%) CH₄/Ar. ^bReaction conditions: 973 K, 95/5 (v/v%) CH₄/N₂.

higher Mo loadings (4–5 wt % Mo; Mo/Al > 0.45) in the Mo-CHA materials used in prior studies, which have been observed (on Mo-MFI) to favor the formation of inactive aluminum molybdates, sublimation of Mo species, and formation of MoO_x clusters ultimately leading to lower aromatic yields. ^{34,35}

H₂ yields measured on Mo-CHA as it deactivates during a single DHA run (Figure 2b) were comparable to analogous H₂ yields on Mo-MFI in similar methane conversion ranges, which

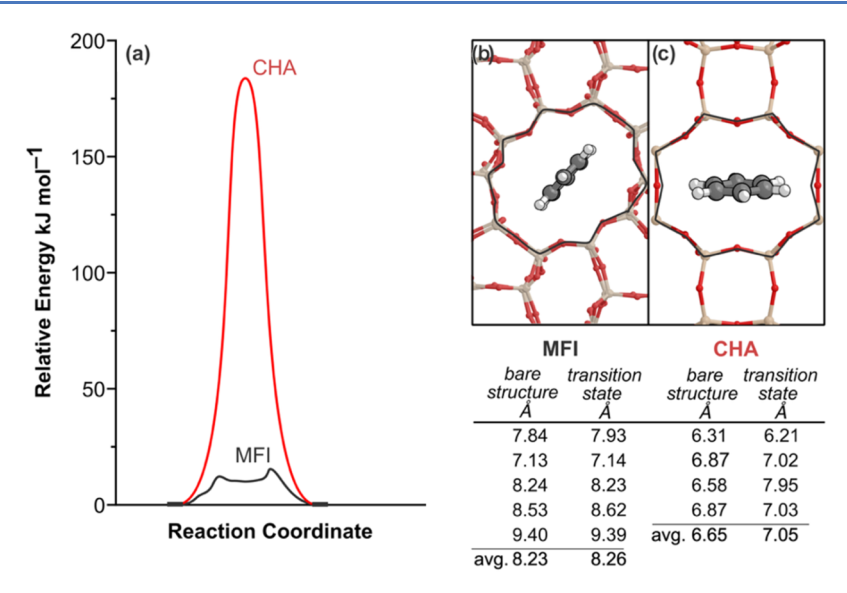


Figure 3. (a) Diffusion barriers for benzene in siliceous forms of MFI (black), CHA (red), and frameworks. Diffusion transition states, along with illustrations of pore restructuring for (b) MFI and (c) CHA. For clarity, images only display a few framework atoms, not the full unit cell. O–O distances between adjacent oxygen atom pairs in 8-MR CHA and 10-MR MFI zeolites are measured from the center to center of each oxygen atom. Values for the bare structure represent O–O dimensions in the absence of benzene, while transition state values demonstrate pore restructuring during benzene diffusion.

is consistent with observations reported by Agote-Arán et al. The yields of both C_2 products (i.e., ethane and ethene; Figure 2c) and of benzene are, respectively, $\sim 1.3 \times$ and $5-6 \times$ lower on Mo-CHA than Mo-MFI (Figure 2c). Moreover, aromatic formation rates (per Mo) and gas-phase carbon balance values measured on Mo-CHA are $\sim 5 \times$ and $\sim 4 \times$ lower, respectively, compared to values measured on Mo-MFI at similar reaction conditions (Table S2, Supporting Information). We attribute these results to diffusion constraints imposed by the small 8-MR windows of CHA (0.38 nm diam.) to larger aromatic molecules (e.g., benzene kinetic diameter ~ 0.59 nm), which would facilitate formation of polyaromatics that remain occluded within crystallites but weakly influence measured rates of smaller H_2 and C_2 molecules formed earlier in the DHA reaction network. 34,35,52

At first glance, given that the critical diameter of benzene (~0.59 nm) is larger than the diameter of the CHA 8-MR window (~0.38 nm), any benzene that forms at active sites within microporous regions would appear to become trapped within CHA cages, implying that any observed benzene products form at the external surfaces of CHA crystals. Yet, molybdenum carbide clusters on unconfined surfaces lead to low yields to benzene and high yields to coke, as shown by Iglesia and co-workers that coke yields decrease upon passivating external H⁺ sites on MFI zeolites to inhibit the exchange of Mo species at external zeolite surfaces⁵³ and by Zhang et al. that increasing zeolite void size (up to \sim 3 nm in MCM-41) systematically decreases aromatics yields and selectivities.⁵² These data suggest that active sites on unconfined external surfaces favor coke formation because confining voids restrict methane dehydroaromatization reaction networks to terminate at benzene. Instead, we propose that benzene can diffuse (at limited rates) through the CHA framework. Prior literature has described the "flexibility" of zeolite frameworks at high temperatures (>540 K) as shown by molecular dynamics simulations and neutron and X-ray diffraction that evince zeolite cell expansion (or contraction), as further described in Section S6.1 of the SI.54-57 This

flexibility allows for the more facile diffusion of molecules that have a larger critical diameter than the pore-limiting diameter of the zeolite framework, rationalizing the diffusion of Kr (0.36 nm) into SOD zeolite (0.24 nm), 58 1,3,5-tripropylbenzene (0.84 nm) into FAU (0.74 nm), 59 and isobutane (0.5 nm) into CHA (0.38 nm).

We used DFT to estimate the diffusion barrier of benzene through the 8-MR windows of the CHA (0.38 nm). Benzene diffusion through CHA 8-MR windows was estimated to occur with a barrier of 184 kJ mol⁻¹ (Figure 3), a very large barrier as expected from the large (relative to 8-MR windows) and rigid nature of benzene, albeit lower than the barrier (248 kJ mol⁻¹) in a prior literature report.⁶¹ Indeed, the structure of the benzene diffusion transition state, as isolated by DFT, shows that the zeolite framework must distort, evident in the average O-O distance across the 8-MR window that increases from 6.6 Å in the absence of benzene to 7.0 Å at the benzene diffusion transition state (Figure 3c). The 8-MR window also changes shape, as the vector parallel to benzene extends to nearly 8 Å (expanding by 1.4 Å), while the normal vector contracts from 6.3 to 6.2 Å, a distortion that causes the window to adopt an elliptical shape (eccentricity of 0.62) that more closely resembles that of benzene (Figure 3c). This barrier through an 8-MR window is, as expected, far larger than the diffusion barrier for benzene in the 10-MR channels of MFI in either the straight (13 kJ mol⁻¹) or sinusoidal (52 kJ mol⁻¹) channels.⁶²

While these diffusion barriers are very large, nonoxidative methane dehydroaromatization reaction temperatures are high (950 K), and the expected kinetic barriers for methane DHA are likely greater than 200 kJ mol⁻¹ for critical (ratecontrolling) steps. Furthermore, benzene diffusion may only need to occur a single time to egress from a CHA cage when active sites are confined within CHA crystallites but in cages that are adjacent to crystallite external surfaces. From these barriers (Figure 3), we can estimate the diffusion coefficient for benzene diffusion through the CHA 8-MR window at reaction temperature (950 K) using a lattice hop equation (details in

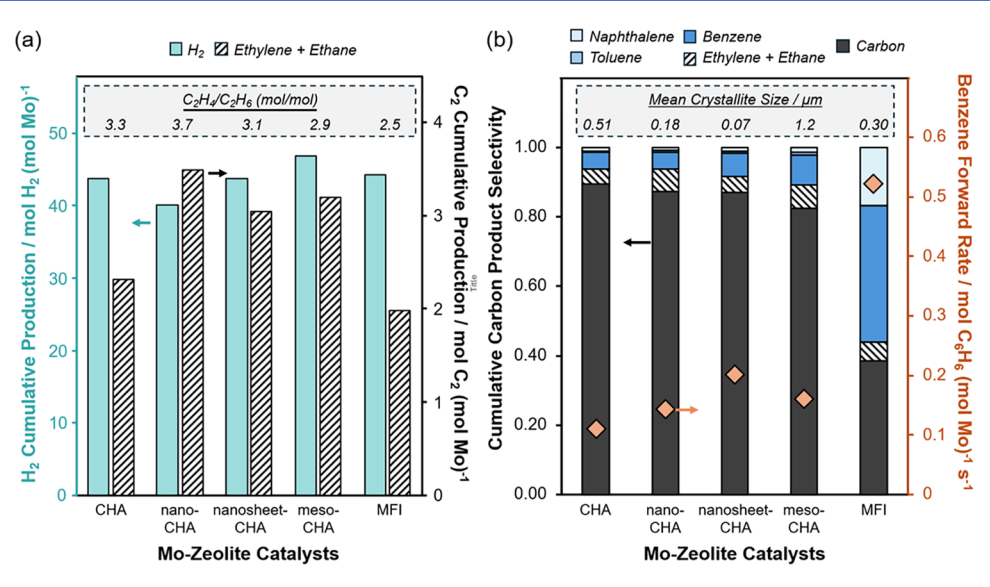


Figure 4. (a) H_2 (turquoise) and C_2 (ethene + ethane, inset shows ratio of C_2H_4 to C_2H_6 ; black diagonal hashing) cumulative production (per Mo) and (b) initial benzene forward rate (per Mo) and cumulative product distribution measured on Mo supported on CHA, nano-CHA, nanosheet-CHA, meso-CHA, and -MFI at ~58 turnovers (inset shows mean crystallite size of each zeolite support). Reaction conditions: 950 K, 90/10% CH_4/Ar (v/v%), 110 kPa total pressure, 12.2 mol of Mo·s (mol of CH_4)⁻¹.

Section S6.2 of the Supporting Information).⁶² The estimated diffusion coefficient is on the same order of magnitude (~10⁻¹⁵ m² s⁻¹) as the diffusion coefficient measured experimentally for *para-xylene* in MFI zeolites at 373 K⁶³ and comparable to *ortho-* and *meta-xylene* self-diffusion coefficients determined by DeLuca and Hibbitts using DFT-calculated diffusion barriers for MFI at 373 K (comparison in Table S3, Supporting Information),⁶² suggesting that benzene diffusion rates should be measurable in CHA at 950 K. Thus, we propose that DHA reactions occur at Mo active sites confined within CHA micropores to form benzene, at measured rates that are strongly limited by intraparticle mass transport.

3.3. Influence of CHA Crystallite Size and Morphology on Methane DHA Reactivity and Selectivity. Estimates of the Weisz-Prater (WP) criterion (Section S6.3, Supporting Information) suggest that aromatic formation rates in CHA are limited by intracrystallite diffusion (WP $\sim 10^1$) even within nanosized zeolite crystallites, to a greater extent compared to MFI zeolites (WP $\sim 10^{-4}$). Restricted intrazeolite diffusion of aromatics should cause measured rates of benzene formation to increase with decreasing CHA crystallite size or by modifying crystallite morphology to introduce mesoporosity. We thus synthesized CHA zeolites with different crystallite sizes and morphologies by adding organic surfactants 64,65 during hydrothermal synthesis to obtain smaller crystallites (nano-CHA), in addition to nanosheet (nanosheet-CHA) and mesoporous morphologies (synthesis details in Section S1 and characterization in Section S7, Supporting Information), and compared them to CHA zeolites synthesized without a surfactant (CHA). Mean crystallite sizes of nano-CHA and CHA were ~182 and ~514 nm, respectively (SEM images in Figures S17 and S18, Supporting Information). XRD patterns of nanosheet-CHA (Figure S16, Supporting Information) show significant peak broadening indicative of smaller crystallites compared to CHA, while Ar adsorption-desorption isotherms of nanosheet-CHA (Figure S15c, Supporting Information) show a hysteresis in the desorption branch, as observed for microporous materials with plate-shaped crystals

that lead to interparticle capillary condensation. 66,67 Mesoporecontaining CHA (meso-CHA) shows a hysteresis during Ar adsorption—desorption isotherms at $P/P_0 \sim 0.5-0.8$, which corresponds to capillary condensation in mesopores (Figure S15d, Supporting Information). SEM images (Figure S19, Supporting Information) show that the nanosheet-CHA morphology comprises agglomerated plate-shaped crystallites of 10-40 nm and larger cubic-shaped crystals (80 to 160 nm), while SEM images of meso-CHA (Figure S20, Supporting Information) show larger crystallites (mean size of $\sim 1.2 \mu m$) with rough surfaces corresponding to mesopores. The fraction of framework Al (per total Al) was estimated by calculating H⁺/Al values¹⁹ for CHA zeolites (Table S5, Supporting Information) and determined to be between 0.58 and 0.62. Next, molybdenum (\sim 1.9–2.8 wt %) was dispersed onto nano-CHA, nanosheet-CHA, meso-CHA, and a reference Mo-MFI using the same procedure used to prepare Mo-CHA (Table S6, Supporting Information), followed by methane DHA kinetic evaluation.

The cumulative production (per Mo), or turnover number (TON), of H₂ and of gaseous and deposited carbon species was measured on Mo-zeolites, and the carbon product selectivity does not change significantly after ~50 turnovers (Figure S12, Supporting Information). Therefore, we compare H₂ production (per Mo; Figure 4a) and cumulative product distribution (Figure 4b) at ~58 turnovers across Mo-CHA zeolites of varying crystallite size and Mo-MFI. The cumulative H_2 and C_2 production (per Mo; Figure 4a), at equivalent turnover number, is comparable for all Mo-CHA and Mo-MFI catalysts, indicating that DHA-active Mo sites in CHA are similar to those in MFI and form H₂ and C₂ products at similar rates. Moreover, the ratio of ethene-to-ethane varies between 2.5 and 3.7 for all catalysts tested (inset of Figure 4a), including Mo-MFI. Since approach-to-equilibrium values for methane-to-ethane and ethane-to-ethene reactions are near unity for all catalysts during deactivation (Figure S6, Supporting Information), we posit that this ratio is solely determined by the equilibrium concentrations of ethane and ethene, in addition to the rate of ethene consumption to form

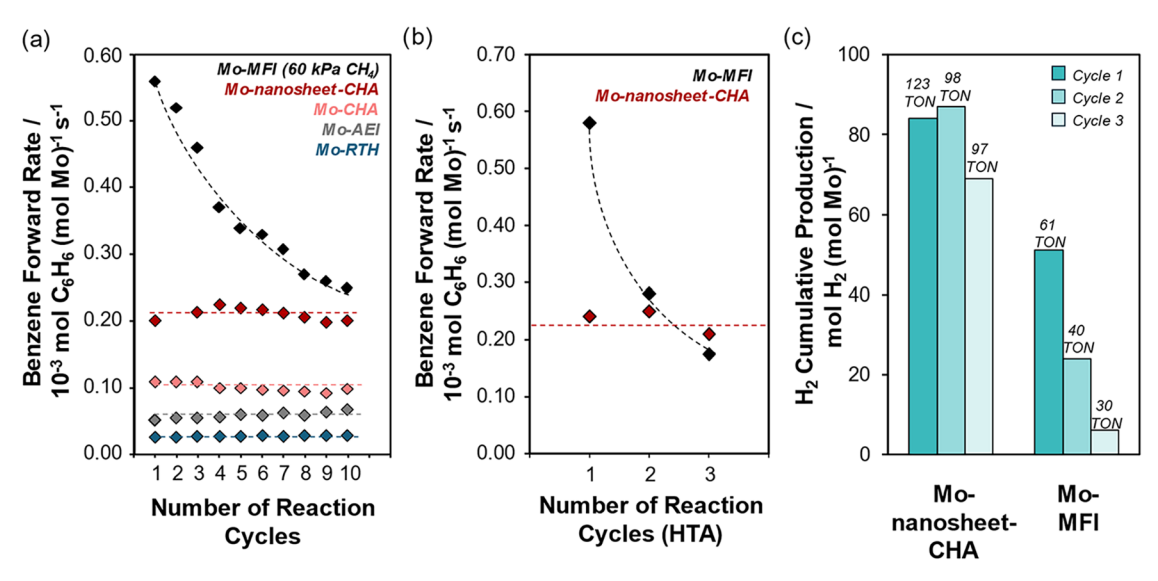


Figure 5. (a) Initial benzene forward rate (per Mo) of Mo-MFI (black diamonds, 60 kPa CH₄) adapted from Santiago-Colón and Gounder¹³ Copyright 2024 Journal of Catalysis, ¹³ Mo-nanosheet-CHA (dark red diamonds), Mo-CHA (light red diamonds), Mo-AEI (gray diamonds), and Mo-RTH (blue diamonds) measured after successive methane DHA reaction cycles with intervening regeneration (20 kPa O₂, 823 K, >6 h). Reaction conditions: 950 K, 90 kPa CH₄, 110–115 kPa total pressure, 9.5–12 mol Mo·s (mol CH₄)-1. (b) Initial benzene forward rate (per Mo) of Mo-MFI (black diamonds) and Mo-nanosheet-CHA (red diamonds) measured after successive reaction cycles (with intervening HTA regeneration at 20 kPa H₂O, 923 K, 8 h); dashed lines are shown to guide the eye. (c) Cumulative H₂ production (per Mo) and total turnover number during the first 3 h of methane DHA measured on Mo-MFI and Mo-nanosheet-CHA after successive reaction cycles with intervening HTA regeneration.

aromatics. In other words, for both Mo-CHA and Mo-MFI catalysts under the conditions studied, these reactions in the DHA network remain equilibrated during deactivation, leading to similar C_2 formation rates. Furthermore, the carbon selectivity to gaseous C_2 products (Figure S13, Supporting Information) is \sim 5× higher on Mo-CHA than on Mo-MFI. Modeling of envisioned industrial methane DHA process performed by Huang et al. shows that ethene selectivity in the hydrocarbon products is directly proportional to the net present value (NPV), improving process economic feasability. Taken together, these findings indicate that small-pore Mo-zeolites offer an attractive route to selectively form H_2 and ethene from methane, if so desired.

Initial rates of benzene formation decrease with the CHA crystallite size (Figure 4b), consistent with rates dependent on intracrystallite diffusion limitations. Rates on Mo-meso-CHA, however, are similar to rates measured on Mo-nanosheet-CHA despite crystallites that are ~10× larger. These data demonstrate that both decreasing the crystallite size or modifying the zeolite morphology to introduce mesoporosity are effective strategies to increase aromatics formation rates by alleviating intrazeolite diffusion limitations. 52,53 Cumulative carbon product selectivity profiles (through 58 TON) measured on Mo-CHA and Mo-MFI catalysts are shown in Figure 4b. The carbon selectivity profile for Mo-MFI is consistent with results from previous studies performed on Mo-MFI with relatively low Mo content (1-2 wt % Mo). 10,34,69 Moreover, carbon product selectivity profiles show that coke content decreases slightly for both Monanosheet-CHA and Mo-meso-CHA compared to Mo-CHA, suggesting that alleviating intracrystalline diffusional constraints allows aromatics to egress from CHA crystallites before further reacting to form coke. These data also allow rationalizing results by Agote-Arán et al., who synthesized CHA crystallites ~10 µm in size and measured benzene

selectivity <3%, which is >4× lower than our reported selectivities.³⁵ The higher (by $\sim 1.5-2\times$) amounts of carbon deposited on Mo-CHA than Mo-MFI likely also reflect topological differences between these two materials due to the cage-like cavities of CHA (~0.74 nm) that are larger than the largest void in MFI (~0.64 nm) and favor formation of polyaromatic carbonaceous deposits (additional discussion in Section S8 of the Supporting Information). In summary, the data shown in Figure 4a,b demonstrate that the zeolite framework does not influence the extent of the dehydroaromatization reactions, as evidenced by equal H₂ and C₂ production rates; rather, the framework presents pore-limiting rings that impose diffusional constraints to increase intracrystalline residence times of aromatic products that are precursors to form polyaromatic carbonaceous deposits and presents spatial constraints via available cavity sizes that influence the sizes of polyaromatic carbonaceous deposits that can form.

3.4. Assessment and Evaluation of Mo-Zeolite Stability during Methane DHA Cycling Operation. To evaluate Mo-zeolite stability during reaction—regeneration cycles, we simulated cyclic reaction—regeneration operation (detailed in Section 2.3) used in our previous work¹³ that allowed us to simulate Mo-MFI catalyst deactivation in a laboratory time scale and serves as a protocol to evaluate and compare the intrinsic material stability of methane DHA catalysts during long-term operation.

Initial forward rates of benzene formation after consecutive methane DHA reaction—regeneration cycles (up to 10) are shown in Figure 5a. Rates on Mo-MFI decrease systematically with increasing numbers of reaction—regeneration cycles¹³ but remain invariant on Mo-CHA and Mo-nanosheet-CHA. Rates measured on Mo-meso-CHA also remained invariant over six reaction—regeneration cycles (Figure S22, Supporting Information). Considering Mo-MFI catalyst deactivation during

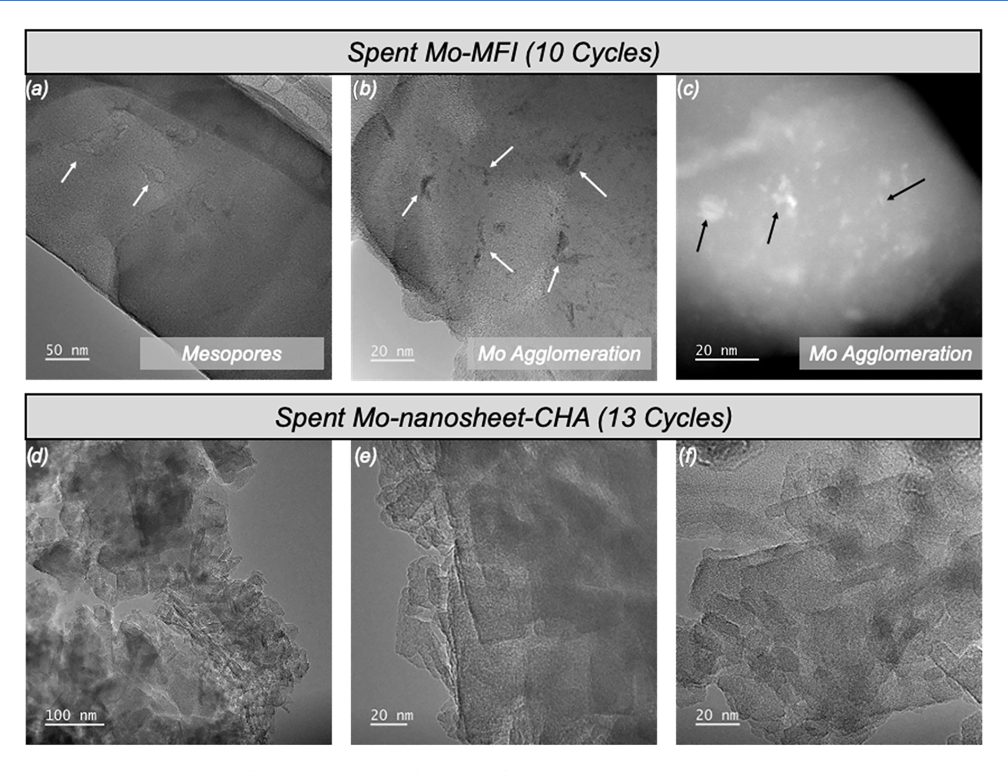


Figure 6. High-resolution TEM images of (a) spent Mo-MFI (10 cycles), white arrows pointing to mesopores in zeolite support, (b) spent Mo-MFI (10 cycles), white arrows pointing to Mo agglomeration in zeolite support, (c) spent Mo-MFI (10 cycles) image obtained in annular dark field mode, black arrows pointing to Mo agglomeration in zeolite support, and (d-f) spent Mo-nanosheet-CHA (13 cycles).

DHA cycles is initiated by the hydrolysis of framework Al with water generated during regeneration, we also measured rates on catalysts regenerated in the presence of water (20 kPa H₂O) at ~100 K higher temperatures (923 K) to accelerate zeolite degradation. 46,47 This aggressive hydrothermal aging protocol (923 K, 20 kPa H₂O, 8 h) exposes both catalysts to equivalent degradation conditions and allows the assessment of catalyst stability during regeneration. Measured rates (per Mo) show only a slight decrease (~15%) on Mo-nanosheet-CHA after three such cycles, but a more significant decrease (>70%) on Mo-MFI that eventually becomes lower than the rates on Mo-nanosheet-CHA (Figure 5b). Figure 5c shows that the cumulative H₂ production (per Mo) and total carbon TON measured during the first 3 h of methane DHA only decrease slightly (~20-25%) in Mo-nanosheet-CHA but decrease by ~90% and 50% on Mo-MFI, respectively, after three aging cycles. These data demonstrate the improved structural durability of CHA over MFI zeolites upon long-term exposure to methane DHA reaction-regeneration cycles.

According to our previous work, invariant initial rates on Mo-CHA suggest that the number of Mo active site precursors does not decrease with successive reaction—regeneration cycles and, in turn, that zeolitic framework Al and associated H⁺ sites in CHA remain intact after exposure to hydrothermal aging conditions. ¹³ We therefore characterized a representative Monanosheet-CHA and Mo-MFI catalyst before and after 10 cycles of methane DHA reaction—regeneration cycles, using protocols for NH₃ titration of H⁺ sites developed for Mozeolites. ¹³ Residual H⁺ sites (Table S7; desorption profiles in Figures S23 and S24, Supporting Information) decrease by ~75% for Mo-MFI but only decrease by ~35% for Monanosheet-CHA, consistent with prior reports of CHA being more structurally durable than MFI after exposure to hydrothermal aging conditions (>723 K, 10 kPa H₂O). ¹⁵

Thus, framework Al and associated H⁺ sites in CHA available for Mo redispersion are not as readily destroyed upon hydrothermal aging as in MFI. H2 TPR of fresh and spent Mo-zeolites was used to evaluate Mo structural changes after the DHA reaction-regeneration cycles. The total H₂ consumed (per Mo) and the fraction of H₂ consumed in the high-temperature feature (per total H₂ consumed), representative of ion-exchanged Mo species, remained invariant in Monanosheet-CHA (Figure S26, Supporting Information) after >10 cycles, indicating that the amount and nature of ionexchanged Mo did not change after DHA reactionregeneration cycles. In contrast, comparison of the H₂ TPR profiles of Mo-MFI after 10 reaction-regeneration cycles shows significant decrease in the H₂ consumed at high temperature (per Mo; 0.50 to 0.29) and total H₂ consumed (per Mo; 2.86 to 2.05; Figure S25, Supporting Information)¹³ and is a consequence of the structural changes of Mo to form aluminum molybdates that do not reduce. These changes cannot be detected using XAS, as evidenced from our EXAFS analysis of fresh and spent Mo-MFI (Figure S3, Supporting Information), where a single feature is observed at ~ 1.2 Å for both materials.

HRTEM images of these Mo-zeolites were collected to observe structural changes after DHA reaction—regeneration cycles. Figure 6a,b shows HRTEM of spent Mo-MFI after 10 cycles, evincing formation of mesopores and agglomerated Mo domains that were not present in the fresh material (Figure S27, Supporting Information). Sintering of Mo particles can be further observed by annular dark (Figure 6c) and bright field (Figure S28, Supporting Information) STEM images that show brighter (and darker) spots corresponding to heavier (by atomic weight) Mo particles, consistent with TEM imaging of Mo-MFI (2 wt. %) after one reaction—regeneration cycle reported by Ismagilov et al. ⁷⁰ In sharp contrast, no structural

changes were observed in HRTEM of spent Mo-nanosheet-CHA (Figure 6d-f), indicating negligible structural degradation of Mo-nanosheet-CHA after exposure to hydrothermal aging conditions. Taken together, these characterization data show that preservation of the zeolitic structure, specifically the framework Al and associated H^+ sites, upon hydrothermal aging conditions is a requirement to enable reversible regeneration of Mo-zeolite materials. Extraction of framework Al sites to form extra-framework Al moieties enables their reactions with Mo species to form inactive aluminum molybdates and other processes that lead to irreversible structural changes and deactivation. Scheme 1 illustrates the

Scheme 1. Structural Changes Characteristic of Mo-MFI (top) and Mo-CHA (bottom) during Regeneration Conditions Illustrating Formation of Inactive Aluminum Molybdates in Mo-MFI (i.e., Irreversible Deactivation) and Interconversion of Molybdenum (Oxy-)Carbide Clusters and Ion-Exchanged Mo Sites in Mo-CHA (i.e., Reversible Deactivation)

structural changes characteristic of Mo-MFI and Mo-CHA during regeneration treatments as examples of irreversible and reversible catalyst deactivation, respectively.

The improved hydrothermal stability of CHA has also been reported for other small-pore zeolite such as RTH, AEI, and LEV, wherein exposure to hydrothermal aging conditions (1073 K, 10 kPa H₂O, 16 h) leads to negligible changes in micropore volume and crystallinity measured by XRD. 18 Thus, to demonstrate the generality of this catalyst design strategy, we synthesized Mo-RTH and Mo-AEI (synthesis and characterization details in Sections S1 and S12, Supporting Information) and measured initial benzene formation rates on Mo-RTH and Mo-AEI, which were $\sim 3.5 \times$ and $\sim 1.5 \times$ lower than rates measured on Mo-CHA, respectively (additional discussion in Section S13 of the Supporting Information). We surmise that differences in measured rates reflect the combined effect of the diffusional constraints imposed by the zeolite and the zeolite void (cavity) size. As discussed in Section S8 of the Supporting Information, larger zeolite void cavities favor reactions of aromatics to coke, which would explain the lower measured rates in Mo-RTH (cavity size ~0.81 nm) than in Mo-CHA (cavity size ~0.74 nm). For Mo-AEI, with a similar void size as CHA, we hypothesize that the lower measured rates reflect differences in diffusional constraints (e.g., crystallite size, tortuosity) which, as we have shown,

influence measured rates. Initial rates, however, do not decrease during successive reaction—regeneration cycles (Figure 5a), as also observed for Mo-CHA, suggesting that framework Al and associated H⁺ sites in the RTH and AEI topologies remain similarly stable through methane DHA reaction and regeneration cycles.

3.5. Effects of H_2 Cofeed on Mo-CHA Carbon Selectivity. H_2 cofeeds (3-9% (v/v)) during methane DHA on Mo-MFI catalysts have been reported to decrease naphthalene formation rates and carbonaceous deposits (i.e., coke) accumulation, leading to increased carbon selectivity to benzene and slower deactivation during a single reaction cycle. ^{12,21} Figure 7 shows the cumulative carbon selectivity and

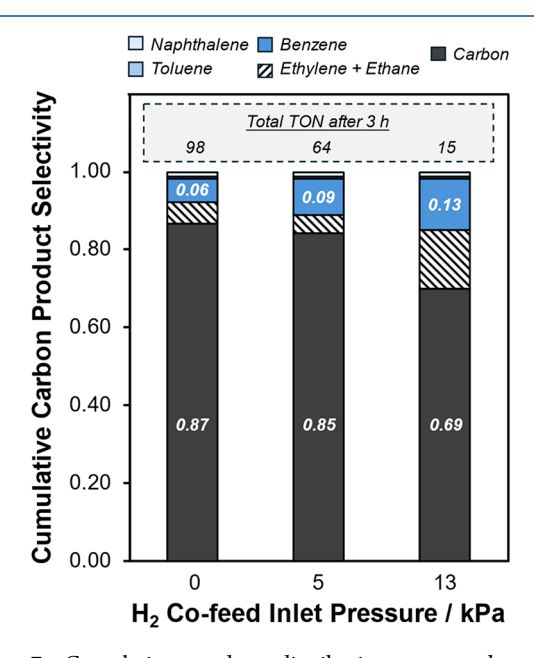


Figure 7. Cumulative product distribution measured on Monanosheet-CHA during first 3 h of methane DHA with varying $\rm H_2$ cofeed pressure (0–13 kPa $\rm H_2$). Inset shows the total carbon TON after 3 h for each catalyst. Reaction conditions: 950 K, 108 kPa total pressure, 12.2–29 mol Mo·s (mol CH₄)⁻¹.

total TON measured on Mo-CHA with H₂ cofeed (0–13 kPa) after 3 h of methane DHA. The cumulative coke selectivity decreases systematically with increasing inlet H2 pressure, while benzene and ethylene selectivities increase. This behavior may reflect H₂ suppressing coke formation via hydrogenation of aromatic precursors to coke²¹ or H₂ reactions with carbonaceous deposits formed during methane DHA to form ethene and methane.⁷¹ The number of total turnovers (inset Figure 7), however, decreases with increasing cofed H₂ cofeed pressure, consistent with H2 inhibiting net benzene formation rates due to the thermodynamic reversibility of methane DHA at reaction conditions (950 K, 90 kPa CH₄).⁷² The relatively high selectivity to coke even at 13 kPa of H₂ might reflect the lower reactivity of polyaromatic carbonaceous deposits with H₂, as demonstrated by Han et al., who performed regenerations of Mo-MFI zeolites in H₂ atmosphere (to 973 K) and observed incomplete removal of carbonaceous deposits formed during DHA.^{4,11} Adding a second metal function (e.g., Pt, Rh, Fe) to Mo-zeolite catalysts to increase the reactivity of H₂ toward hydrogenating carbonaceous deposits might provide an alternative strategy to mitigate their formation or assist in their decomposition.

Jung et al. performed a techno-economic analysis for various scenarios of methane DHA industrial applications, including cofeeding H₂ (5% (mol/mol)), which can be provided from the H₂ generated during reaction. These authors showed that H₂ cofeeding plays a complex role in the economics of the process since it lowers production rates but increases BTX selectivity, but still results in positive net present values, indicating the economic viability of such a process. Moreover, the catalyst replacement time, which has a negative effect on the process economics, was set to 6 months for Mo-MFI. Therefore, since H₂ yields are equal in Mo-MFI and Mo-CHA, in potential DHA applications, the H₂ produced during methane DHA could be recycled as cofeed to influence carbon selectivity and moderate the formation of surface carbonaceous deposits prior to regeneration treatments of Mo-CHA catalysts.⁷⁴ We surmise that the replacement time for fully regenerable Mo-CHA catalysts would be much longer than that for Mo-MFI, facilitating the implementation of an industrial DHA application.

4. CONCLUSIONS

Development of commercial methane DHA applications requires improvement in long-term catalyst stability, given that typically used Mo-MFI materials irreversibly deactivate upon successive reaction-regeneration cycles. In this work, we design and interrogate a family of small-pore zeolite supports for Mo that have been shown to more effectively retain their structural integrity upon exposure to hydrothermal aging conditions compared to medium-pore frameworks such as MFI. Spectroscopic and quantitative H₂ TPR characterization provide evidence that ion-exchanged Mo species are formed on CHA and other small-pore zeolite supports during hightemperature air treatment (>823 K) and resemble the ionexchanged Mo complexes formed on MFI. These species undergo carburization upon exposure to methane (950 K) to form Mo (oxy-)carbides that catalyze methane DHA to form H₂ and C₂ products (ethane, ethene) at nearly identical yields on Mo-CHA and Mo-MFI. These data suggest that the Mo active site precursor structure and active site reactivity are not significantly affected by the zeolite framework.

DFT was used to estimate benzene diffusion barriers through CHA 8-MR windows (184 kJ mol⁻¹) and calculate diffusion coefficients, which were determined to be on the same order of magnitude as the diffusion coefficients of para-, meta-, and ortho-xylene in MFI at 373 K measured experimentally and estimated by DFT. These data support the concept that zeolite frameworks become flexible at high temperatures, allowing for the diffusion of molecules that have kinetic diameters larger than the nominal zeolite pore window. Zeolite topology, however, influences DHA rates and selectivities through the combined effect of void size and diffusional constraints on aromatic products that cause such products to undergo further dehydrogenation to form coke inside the zeolite micropores. Aromatics formation rates and yields approach values (within 4x) of Mo-MFI for CHA zeolites with crystallite sizes that are ~10-40 nm in size or on mesopore-containing CHA zeolites, which alleviate intracrystallite diffusion constraints for aromatic products. Cumulative coke selectivity measured on Mo-CHA is higher compared to Mo-MFI but decreases with decreasing CHA crystallite size and in mesoporous-CHA. Moreover, H2 cofeeds decrease coke selectivity, providing a route to adjust DHA reaction conditions to increase carbon selectivity to gaseous

products prior to the next regeneration treatment that is invariably required.

Quantitative site characterization data combined with highresolution microscopy provide compelling evidence that smallpore eight-membered-ring (8-MR) zeolite support retains its structural integrity upon exposure to high-temperature hydrothermal aging conditions during catalyst regeneration, in contrast to medium-pore zeolites like MFI. Therefore, smallpore zeolite supports allow for the reversible recovery of dispersed, ion-exchanged Mo species that serve as precursors to DHA-active sites, resulting in invariant methane DHA rates and product yields upon successive regeneration treatments and eventually to higher rates (per Mo) than Mo-MFI. Although yields and selectivities remain lower compared to Mo-MFI, we identify crystal and reaction engineering strategies that can be further studied to optimize catalyst performance metrics in fully regenerable materials. These findings provide new catalyst design routes to prolong the useful lifetime of Mozeolites used for nonoxidative methane conversion and demonstrate the efficacy of small-pore zeolites to produce H₂ and C₂ hydrocarbons in industrial applications.

ASSOCIATED CONTENT

Supporting Information

The Supporting Information is available free of charge at https://pubs.acs.org/doi/10.1021/acscatal.5c04775.

Zeolite synthesis recipes, zeolite characterization methods (XRD, Ar micropore volume measurements, H_2 TPR, NH_3 gas titration, in situ XAS, SEM, and HRTEM), supplemental kinetic data and discussion, supplemental discussion on benzene diffusion through CHA pore window, and supplemental discussion on influence of zeolite topology on DHA selectivity (PDF)

AUTHOR INFORMATION

Corresponding Author

Rajamani Gounder — Charles D. Davidson School of Chemical Engineering, Purdue University, West Lafayette, Indiana 47907, United States; orcid.org/0000-0003-1347-534X; Email: rgounder@purdue.edu

Authors

Angel N. Santiago-Colón — Charles D. Davidson School of Chemical Engineering, Purdue University, West Lafayette, Indiana 47907, United States

Hien Pham – Department of Chemical and Biological Engineering, University of New Mexico, Albuquerque, New Mexico 87131-0001, United States

Ayotunde Alabi — Charles D. Davidson School of Chemical Engineering, Purdue University, West Lafayette, Indiana 47907, United States

David Hibbitts — Charles D. Davidson School of Chemical Engineering, Purdue University, West Lafayette, Indiana 47907, United States; © orcid.org/0000-0001-8606-7000

Abhaya Datye — Department of Chemical and Biological Engineering, University of New Mexico, Albuquerque, New Mexico 87131-0001, United States; orcid.org/0000-0002-7126-8659

Complete contact information is available at: https://pubs.acs.org/10.1021/acscatal.5c04775

Notes

The authors declare no competing financial interest.

ACKNOWLEDGMENTS

We acknowledge the support for this work provided by the National Science Foundation under Cooperative Agreement No. EEC-1647722, an Engineering Research Center for the Innovative and Strategic Transformation of Alkane Resources (CISTAR). A.S.C. acknowledges support from the National Science Foundation under the Graduate Research Fellowship (GRFP) under grant number DGE-1842166. Use of the Advanced Photon Source (APS) at Argonne National Lab is supported by the U.S. Department of Energy, Office of Science, and Office of Basic Energy Sciences, under contract no. DE-AC02-06CH11357. MRCAT operations and beamline 10-BM are supported by the Department of Energy and the MRCAT member institutions. This research used beamline 8-ID (ISS) of the National Synchrotron Light Source II, a U.S. Department of Energy (DOE) Office of Science User Facility operated for the DOE Office of Science by Brookhaven National Laboratory under Contract No. DE-SC0012704. We thank Sachem, Inc., for providing the organic structuredirecting agent used to synthesize SSZ-13 (CHA) and SSZ-39 (AEI). We also thank Diamarys Salomé-Rivera (Purdue) for SEM imaging of CHA zeolites and Tania Class-Martínez (Purdue) for performing HTA regeneration protocols. We thank Ryoh-Suke Sekiya and Bereket Bekele (Purdue) for providing a critical review of this manuscript.

REFERENCES

- (1) Wang, D.; Lunsford, J. H.; Rosynek, M. P. Catalytic Conversion of Methane to Benzene over Mo/ZSM-5. *Top. Catal.* **1996**, 3, 289–297.
- (2) Weckhuysen, B. M.; Wang, D.; Rosynek, M. P.; Lunsford, J. H. Conversion of Methane to Benzene over Transition Metal Ion ZSM-5 Zeolites: I. Catalytic Characterization. *J. Catal.* **1998**, *175* (2), 338–346.
- (3) Wang, L.; Tao, L.; Xie, M.; Xu, G.; Huang, J.; Xu, Y. Dehydrogenation and Aromatization of Methane under Non-Oxidizing Conditions. *Catal. Lett.* **1993**, 21, 35–41.
- (4) Zhou, J.; Zhao, J.; Zhang, T.; Ye, M.; Liu, Z. Regeneration of Catalysts Deactivated by Coke Deposition: A Review. *Chin. J. Catal.* **2020**, *41* (7), 1048–1061.
- (5) Kosinov, N.; Hensen, E. J. M. Reactivity, Selectivity, and Stability of Zeolite-Based Catalysts for Methane Dehydroaromatization. *Adv. Mater.* **2020**, 32, No. 2002565.
- (6) Jung, W.; Kim, H.; Lim, Y. H.; Ryu, H. W.; Kim, D. H.; Lee, J. Methane Dehydroaromatization Process in a Carbon-Neutral Strategy. *Energy Convers. Manage.* **2024**, 299, No. 117771.
- (7) Mevawala, C.; Bai, X.; Hu, J.; Bhattacharyya, D. Plant-Wide Modeling and Techno-Economic Analysis of a Direct Non-Oxidative Methane Dehydroaromatization Process via Conventional and Microwave-Assisted Catalysis. *Appl. Energy* **2023**, *336*, No. 120795.
- (8) Jung, W.; Lim, Y. H.; Kim, H.; Kim, D. H.; Lee, J. Kinetic Modeling of Methane Dehydroaromatization over Mo/ZSM-5 Catalysts. *Chem. Eng. J.* **2024**, 496, No. 153616.
- (9) Cook, B.; Mousko, D.; Hoelderich, W.; Zennaro, R. Conversion of Methane to Aromatics over Mo2C/ZSM-5 Catalyst in Different Reactor Types. *Appl. Catal., A* **2009**, 365 (1), 34–41.
- (10) Kosinov, N.; Coumans, F. J. A. G.; Li, G.; Uslamin, E.; Mezari, B.; Wijpkema, A. S. G.; Pidko, E. A.; Hensen, E. J. M. Stable Mo/HZSM-5 Methane Dehydroaromatization Catalysts Optimized for High-Temperature Calcination-Regeneration. *J. Catal.* **2017**, 346, 125–133.
- (11) Han, S. J.; Kim, S. K.; Hwang, A.; Kim, S.; Hong, D. Y.; Kwak, G.; Jun, K. W.; Kim, Y. T. Non-Oxidative Dehydroaromatization of

- Methane over Mo/H-ZSM-5 Catalysts: A Detailed Analysis of the Reaction-Regeneration Cycle. *Appl. Catal., B* **2019**, *241*, 305–318.
- (12) Skutil, K.; Taniewski, M. Some Technological Aspects of Methane Aromatization (Direct and via Oxidative Coupling). Fuel Process. Technol. 2006, 87 (6), 511–521.
- (13) Santiago-Colón, Á. N.; Gounder, R. Structural Changes to Molybdenum and Brønsted Acid Sites in MFI Zeolites during Methane Dehydroaromatization Reaction-Regeneration Cycles. *J. Catal.* **2024**, 430, No. 115335.
- (14) Portilla, M. T.; Llopis, F. J.; Martínez, C. Non-Oxidative Dehydroaromatization of Methane: An Effective Reaction-Regeneration Cyclic Operation for Catalyst Life Extension. *Catal. Sci. Technol.* **2015**, *5*, 3806–3821.
- (15) Fickel, D. W.; D'Addio, E.; Lauterbach, J. A.; Lobo, R. F. The Ammonia Selective Catalytic Reduction Activity of Copper-Exchanged Small-Pore Zeolites. *Appl. Catal., B* **2011**, *102* (3–4), 441–448
- (16) Ye, Q.; Wang, L.; Yang, R. T. Activity, Propene Poisoning Resistance and Hydrothermal Stability of Copper Exchanged Chabazite-like Zeolite Catalysts for SCR of NO with Ammonia in Comparison to Cu/ZSM-5. *Appl. Catal., A* **2012**, *427*–428, 24–34.
- (17) Di Iorio, J. R.; Gounder, R. Controlling the Isolation and Pairing of Aluminum in Chabazite Zeolites Using Mixtures of Organic and Inorganic Structure-Directing Agents. *Chem. Mater.* **2016**, 28 (7), 2236–2247.
- (18) Albarracin-Caballero, J. D.; Khurana, I.; Di Iorio, J. R.; Shih, A. J.; Schmidt, J. E.; Dusselier, M.; Davis, M. E.; Yezerets, A.; Miller, J. T.; Ribeiro, F. H.; Gounder, R. Structural and Kinetic Changes to Small-Pore Cu-Zeolites after Hydrothermal Aging Treatments and Selective Catalytic Reduction of NOx with Ammonia. *React. Chem. Eng.* 2017, 2, 168.
- (19) Di Iorio, J. R.; Bates, S. A.; Verma, A. A.; Delgass, W. N.; Ribeiro, F. H.; Miller, J. T.; Gounder, R. The Dynamic Nature of Bronsted Acid Sites in Cu-Zeolites During NOx Selective Catalytic Reduction: Quantification by Gas-Phase Ammonia Titration. *Top. Catal.* **2015**, *58*, 424–434.
- (20) Leshchev, D.; Rakitin, M.; Luvizotto, B.; Kadyrov, R.; Ravel, B.; Attenkofer, K.; Stavitski, E. The Inner Shell Spectroscopy Beamline at NSLS-II: A Facility for in Situ and Operando X-Ray Absorption Spectroscopy for Materials Research. *J. Synchrotron Radiat.* **2022**, *29*, 1095–1106.
- (21) Tan, P. L.; Wong, K. W.; Au, C. T.; Lai, S. Y. Effects of Co-Fed O2 and CO2 on the Deactivation of Mo/HZSM-5 for Methane Aromatization. *Appl. Catal., A* **2003**, 253 (1), 305–316.
- (22) Schmieg, S. J.; Oh, S. H.; Kim, C. H.; Brown, D. B.; Lee, J. H.; Peden, C. H. F.; Kim, D. H. Thermal Durability of Cu-CHA NH3-SCR Catalysts for Diesel NO x Reduction. *Catal. Today* **2012**, *184*, 252–261.
- (23) Kravchenko, P.; Plaisance, C.; Hibbitts, D. A New Computational Interface for Catalysis; ChemRxiv, 2019.
- (24) Perdew, J. P.; Burke, K.; Ernzerhof, M. Generalized Gradient Approximation Made Simple. *Phys. Rev. Lett.* **1996**, *77*, 3865–3868.
- (25) Hammer, B.; Hansen, L. B.; No, J. K. Improved Adsorption Energetics within Density-Functional Theory Using Revised Perdew-Burke-Ernzerhof Functionals. *Phys. Rev. B* **1999**, *59*, 7413–7421.
- (26) Zhang, Y.; Yang, W. Comment on "Generalized Gradient Approximation Made Simple. *Phys. Rev. Lett.* **1998**, *80*, 890.
- (27) Grimme, S.; Antony, J.; Ehrlich, S.; Krieg, H. A Consistent and Accurate Ab Initio Parametrization of Density Functional Dispersion Correction (DFT-D) for the 94 Elements H-Pu. *J. Chem. Phys.* **2010**, 132, No. 154104.
- (28) Grimme, S.; Ehrlich, S.; Goerigk, L. Effect of the Damping Function in Dispersion Corrected Density Functional Theory. *J. Comput. Chem.* **2011**, 32, 1456–1465.
- (29) Schröder, H.; Creon, A.; Schwabe, T. Reformulation of the D3(Becke–Johnson) Dispersion Correction without Resorting to Higher than C6 Dispersion Coefficients. *J. Chem. Theory Comput.* **2015**, *11*, 3163–3170.

- (30) Monkhorst, H. J.; Pack, J. D. Special Points for Brillouin-Zone Integrations. *Phys. Rev. B* **1976**, *13*, 5188.
- (31) Berne, B. J.; Mills, G.; Jacobsen, K. W. et al. Nudged Elastic Band Method for Finding Minimum Energy Paths of Transitions. In Classical and Quantum Dynamics in Condensed Phase Simulations; World Scientific, 1998; pp 385–404.
- (32) Henkelman, G.; Jónsson, H. A Dimer Method for Finding Saddle Points on High Dimensional Potential Surfaces Using Only First Derivatives. *J. Chem. Phys.* **1999**, *111*, 7010–7022.
- (33) Chen, L. Y.; Lin, L.; Xu, Z.; Li, X.; Zhang, T. Dehydro-Oligomerization of Methane to Ethylene and Aromatics over Molybdenum/HZSM-5 Catalyst. *J. Catal.* **1995**, *157*, 190–200.
- (34) Kosinov, N.; Coumans, F. J. A. G.; Uslamin, E. A.; Wijpkema, A. S. G.; Mezari, B.; Hensen, E. J. M. Methane Dehydroaromatization by Mo/HZSM-5: Mono- or Bifunctional Catalysis? *ACS Catal.* **2017**, 7 (1), 520–529.
- (35) Agote-Arán, M.; Kroner, A. B.; Wragg, D. S.; Sławi Nski, W. A.; Briceno, M.; Islam, H. U.; Sazanovich, I. V.; Rivas, M. E.; Smith, A. W. J.; Collier, P.; Lezcano-González, I.; Beale, A. M.; Valencia, S.; Daou, T. J. Understanding the Deactivation Phenomena of Small-Pore Mo/H-SSZ-13 during Methane Dehydroaromatisation. *Molecules* 2020, 25, 5048.
- (36) Kim, Y. H.; Borry, R. W.; Iglesia, E. Genesis of Methane Activation Sites in Mo-Exchanged H-ZSM-5 Catalysts. *Microporous Mesoporous Mater.* **2000**, 35–36, 495–509.
- (37) Borry, R. W.; Kim, Y. H.; Huffsmith, A.; Reimer, J. A.; Iglesia, E. Structure and Density of Mo and Acid Sites in Mo-Exchanged H-ZSM5 Catalysts for Nonoxidative Methane Conversion. *J. Phys. Chem.* B 1999, 103 (28), 5787–5796.
- (38) Tessonnier, J. P.; Louis, B.; Rigolet, S.; Ledoux, M. J.; Pham-Huu, C. Methane Dehydro-Aromatization on Mo/ZSM-5: About the Hidden Role of Brønsted Acid Sites. *Appl. Catal., A* **2008**, 336 (1–2), 79–88.
- (39) Gao, J.; Zheng, Y.; Jehng, J. M.; Tang, Y.; Wachs, I. E.; Podkolzin, S. G. Identification of Molybdenum Oxide Nanostructures on Zeolites for Natural Gas Conversion. *Science* **2015**, 348 (6235), 686–690.
- (40) Ding, W.; Li, S.; Meitzner, G. D.; Iglesia, E. Methane Conversion to Aromatics on Mo/H-ZSMS: Structure of Molybdenum Species in Working Catalysts. *J. Phys. Chem. B* **2001**, *105* (2), 506–513.
- (41) Li, W.; Meitzner, G. D.; Borry, R. W.; Iglesia, E. Raman and X-Ray Absorption Studies of Mo Species in Mo/H-ZSM5 Catalysts for Non-Oxidative CH4 Reactions. *J. Catal.* **2000**, *191* (2), 373–383.
- (42) Lezcano-González, I.; Oord, R.; Rovezzi, M.; Glatzel, P.; Botchway, S. W.; Weckhuysen, B. M.; Beale, A. M. Molybdenum Speciation and Its Impact on Catalytic Activity during Methane Dehydroaromatization in Zeolite ZSM-5 as Revealed by Operando X-Ray Methods. *Angew. Chem.* **2016**, *128* (17), 5301–5305.
- (43) Razdan, N. K.; Kumar, A.; Foley, B. L.; Bhan, A. Influence of Ethylene and Acetylene on the Rate and Reversibility of Methane Dehydroaromatization on Mo/H-ZSM-5 Catalysts. *J. Catal.* **2020**, 381, 261–270.
- (44) Razdan, N. K.; Bhan, A. Carbidic Mo Is the Sole Kinetically-Relevant Active Site for Catalytic Methane Dehydroaromatization on Mo/H-ZSM-5. *J. Catal.* **2020**, 389, 667–676.
- (45) Molajafari, F.; Hiennadi, E. J.; Khatib, S. J.; Howe, J. D. Evolution, Speciation, and Distribution of Mo Oxides in MFI-Type Zeolites. *J. Phys. Chem. C* **2025**, *129* (11), 5603–5616.
- (46) Imamura, S.; Sasaki, H.; Shono, M.; Kanai, H. Structure of Molybdenum Supported on A-, g-, and x-Aluminas in Relation to Its Epoxidation Activity. *J. Catal.* **1998**, *177*, 72–81.
- (47) Chen, K.; Xie, S.; Bell, A. T.; Iglesia, E. Structure and Properties of Oxidative Dehydrogenation Catalysts Based on MoO3/Al2O3. *J. Catal.* **2001**, 198 (2), 232–242.
- (48) Arnoldy, P.; Jonge, D.; Moulijn, J. A. Temperature-Programmed Reduction of MoO3 and MoO2. *J. Phys. Chem. A* 1985, 89 (21), 4517–4526.

- (49) Kosinov, N.; Wijpkema, A. S. G.; Uslamin, E.; Rohling, R.; Coumans, F. J. A. G.; Mezari, B.; Parastaev, A.; Poryvaev, A. S.; Fedin, M. V.; Pidko, E. A.; Hensen, E. J. M. Confined Carbon Mediating Dehydroaromatization of Methane over Mo/ZSM-5. *Angew. Chem.* **2018**, *130* (4), 1028–1032.
- (50) Zhang, J.-Z.; Long, M. A.; Howe, R. F. Molybdenum ZSM-5 Zeolite Catalysts for the Conversion of Methane to Benzene. *Catal. Today* **1998**, *44*, 293–300.
- (51) Zheng, Y.; Tang, Y.; Gallagher, J. R.; Gao, J.; Miller, J. T.; Wachs, I. E.; Podkolzin, S. G. Molybdenum Oxide, Oxycarbide, and Carbide: Controlling the Dynamic Composition, Size, and Catalytic Activity of Zeolite-Supported Nanostructures. *J. Phys. Chem. C* **2019**, 123 (36), 22281–22292.
- (52) Zhang, C.-L.; Li, S.; Yuan, Y.; Zhang, W.-X.; Wu, T.-H.; Lin, L.-W. Aromatization of Methane in the Absence of Oxygen over Mo-Based Catalysts Supported on Different Types of Zeolites. *Catal. Lett.* **1998**, *56*, 207–213.
- (53) Ding, W.; Meitzner, G. D.; Iglesia, E. The Effects of Silanation of External Acid Sites on the Structure and Catalytic Behavior of Mo/H-ZSM5. *J. Catal.* **2002**, *206* (1), 14–22.
- (54) Smit, B.; Maesen, T. L. M. Molecular Simulations of Zeolites: Adsorption, Diffusion, and Shape Selectivity. *Chem. Rev.* **2008**, *108* (10), 4125–4184.
- (55) Ghojavand, S.; Dib, E.; Mintova, S. Flexibility in Zeolites: Origin, Limits, and Evaluation. *Chem. Sci.* **2023**, *14* (44), 12430–12446.
- (56) Parise, J. B.; Abrams, L.; Gier, E.; Corbin, D. R.; Jorgensen, J. D.; Prince, E. Flexibility of the Framework of Zeolite Rho. Structural Variation from 11 to 573 K. A Study Using Neutron Powder Diffraction Data. *J. Phys. Chem. A* **1984**, *88*, 2303–2307.
- (57) Deem, M. W.; Newsam, J.; Creighton, J. Fluctuations in Zeolite Aperture Dimensions Simulated by Crystal Dynamics. *J. Am. Chem. Soc.* **1992**, *114*, 7198–7207.
- (58) Barrer, R. M.; Vaugitan, D. E. W. Trapping of Inert Gases in Sodalite and Cancrinite Crystals. J. Phys. Chem. Solids 1971, 32, 731–743
- (59) Ruthven, D. M.; Kaul, B. K. Adsorption of Aromatic Hydrocarbons in NaX Zeolite. 2. Kinetics. *Ind. Eng. Chem. Res.* **1993**, 32, 2053–2057.
- (60) Bolshakov, A.; Van Hoof, A. J. F.; Mezari, B.; Kosinov, N.; Hensen, E. A Versatile Mono-Quaternary Ammonium Salt as a Mesoporogen for the Synthesis of Hierarchical Zeolites. *Catal. Sci. Technol.* **2019**, 9 (23), 6737–6748.
- (61) Smith, A. T.; Plessow, P. N.; Studt, F. Density Functional Theory Calculations of Diffusion Barriers of Organic Molecules through the 8-Ring of H-SSZ-13. *Chem. Phys.* **2021**, *541*, No. 111033.
- (62) DeLuca, M.; Hibbitts, D. Predicting Diffusion Barriers and Diffusivities of C6–C12 Methylbenzenes in MFI Zeolites. *Microporous Mesoporous Mater.* **2022**, 333. 111705.
- (63) Mirth, G.; Cejka, J.; Lercher, J. Transport and Isomerization of Xylenes over HZSM-5 Zeolites. *J. Catal.* **1993**, *139*, 24–33.
- (64) Kumar, M.; Luo, H.; Románromán-Leshkov, Y.; Rimer, J. D. SSZ-13 Crystallization by Particle Attachment and Deterministic Pathways to Crystal Size Control. *J. Am. Chem. Soc.* **2015**, *137*, 13007–13017.
- (65) Santiago-Colón, A.; Lee, S.; Gounder, R. Method for Making CHA Zeolites and Zeotypes. U.S. Patent US63/5292642024.
- (66) Sing, K. S. W.; Williams, R. T. Physisorption Hysteresis Loops and the Characterization of Nanoporous Materials. *Adsorpt. Sci. Technol.* **2004**, 22 (10), 773–782.
- (67) Schlumberger, C.; Thommes, M. Characterization of Hierarchically Ordered Porous Materials by Physisorption and Mercury Porosimetry—A Tutorial Review. *Adv. Mater. Interfaces* **2021**, 8 (4), No. 2002181, DOI: 10.1002/admi.202002181.
- (68) Huang, K.; Miller, J. B.; Huber, G. W.; Dumesic, J. A.; Maravelias, C. T. A General Framework for the Evaluation of Direct Nonoxidative Methane Conversion Strategies. *Joule* **2018**, 2 (2), 349–365.

- (69) Beuque, A.; Valtchev, V.; Mintova, S.; Gilson, J. P.; Pinard, L. Identification of Reversible and Irreversible Deactivation of MDA Catalysts: A Key to Design a Viable Process. *J. Catal.* **2023**, 426, 39–51.
- (70) Ismagilov, Z. R.; Matus, E. V.; Ismagilov, I. Z.; Kerzhentsev, M. A.; Zailovskii, V. I.; Dosumov, K. D.; Mustafinc, A. G. Structural Changes of Mo/ZSM-5 Catalysts during the Methane Dehydroaromatization. *Eurasian Chem.-Technol. J.* **2010**, *12* (1), 9–16.
- (71) Lee, S.; Choi, M. Unveiling Coke Formation Mechanism in MFI Zeolites during Methanol-to-Hydrocarbons Conversion. *J. Catal.* **2019**, *375*, 183–192.
- (72) Bedard, J.; Hong, D. Y.; Bhan, A. CH4 Dehydroaromatization on Mo/H-ZSM-5:1. Effects of Co-Processing H2 and CH3COOH. *J. Catal.* **2013**, 306, 58–67.
- (73) Menon, U.; Rahman, M.; Khatib, S. J. A Critical Literature Review of the Advances in Methane Dehydroaromatization over Multifunctional Metal-Promoted Zeolite Catalysts. *Appl. Catal., A* **2020**, *608*, No. 117870.
- (74) Honda, K.; Yoshida, T.; Zhang, Z. G. Methane Dehydroar-omatization over Mo/HZSM-5 in Periodic CH 4-H2 Switching Operation Mode. *Catal. Commun.* **2003**, *4* (1), 21–26.

